Non-ideal Selection Field Induced Artifacts in X-Space MPI

Ecrin Yagiz[a,b*] · Ahmet R. Cagil[a,b] · Emine Ulku Saritas[a,b,c]

[a]Department of Electrical and Electronics Engineering, Bilkent University, Ankara, Turkey
[b]National Magnetic Resonance Research Center (UMRAM), Bilkent University, Ankara, Turkey
[c]Neuroscience Program, Sabuncu Brain Research Center, Bilkent University, Ankara, Turkey
*Corresponding author, email: yagiz@ee.bilkent.edu.tr

Abstract

In magnetic particle imaging (MPI), the selection field deviates from its ideal linearity in regions away from the center of the scanner. This work demonstrates that unaccounted non-linearity of the selection field causes warping in the image reconstructed with a basic x-space approach. We also show that unwarping algorithms can be applied to effectively address this issue, once the displacement map acting on the reconstructed image is determined. The unwarped image accurately represents the locations of nanoparticles, albeit with a resolution loss in regions away from the center of the scanner due to the degradation in selection field gradients.

I. Introduction

In magnetic particle imaging (MPI), the ideal signal is defined via the response of the nanoparticles to an oscillating drive field [1]. A typical simplifying assumption in MPI is that the selection field gradient is constant in the imaging field-of-view (FOV) [2, 3, 4, 5]. Such highly linear gradient fields could be achieved using large magnets and/or additional coils, e.g., similar to shim coils used in magnetic resonance imaging (MRI) to compensate for B_0 field inhomogeneity [6]. However, practical trade-offs such as the total cost of the system may limit these approaches. For the case of system function reconstruction (SFR), the field non-linearity is implicitly taken into account and corrected, at the cost of a very lengthy calibration procedure that incorporates overscanning [7]. For basic x-space reconstruction, geometric warping effects are expected to occur if the FOV extends beyond the linear region [2].

Similar problems have extensively been investigated in MRI, as the non-linearity of the magnetic field gradients cause what is known as "gradient warping" [8, 9]. In MPI, artifacts due to non-ideal selection fields were previously demonstrated for field free line (FFL) MPI with Radon-based and SFR-based reconstructions, although no solutions were suggested [10].

In this work, we perform a simulation-based investigation of selection-field-induced warping and resolution loss for field free point (FFP) MPI with basic x-space reconstruction, together with theoretical derivations of both effects. We show that the warping effects are relatively benign and can be effectively addressed via unwarping algorithms to achieve a geometrically accurate representation of the underlying nanoparticle distribution. The resolution loss cannot be corrected in such a simple fashion, and may be the factor that determines the maximum size of the FOV for a given scanner setup.

II. Material and Methods

Simulations for selection-field-induced-warping were performed in four stages: 1) Magnetic fields were simulated for both the ideal and non-ideal selection field cases. The simulation parameters were based on our in-house prototype FFP MPI scanner that features (2.4, 2.4, -4.8) T/m selection field gradients [11, 12]. 2) Imaging simulations were performed using either the ideal or non-ideal selection fields, followed by x-space MPI reconstruction with DC recovery [13, 14]. 3) The selection-field-induced warping and resolution loss of the MPI image was quantified for each pixel via a displacement map, and compared with theoretical expectations. 4) A potential solution for the warping artifact was implemented via a geometric transformation of the reconstructed images using the displacement maps.

To determine the selection-field-induced resolution loss due to the position-dependent degradation in selection field gradients, images from a non-ideal selection field were investigated with and without image unwarping using the displacement map. To quantify the resolution, full-width-half-maximum (FWHM) values were

measured, and compared with values from x-space theory.

The following sections provide details of each step.

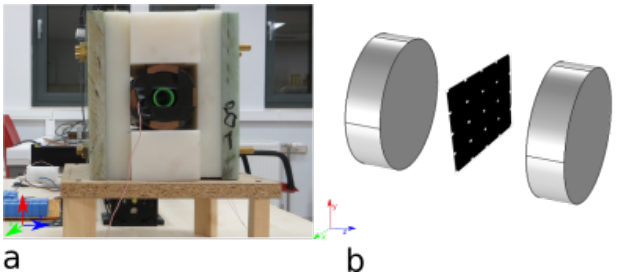

Figure 1: a) In-house FFP MPI scanner with $(2.4, 2.4, -4.8)$ T/m selection field, on which the magnetic field simulations were based. b) The selection field was generated using two permanent disk magnets with 7-cm diameter and 2-cm thickness. For imaging simulations, a 2D phantom with point sources was placed at the center of the magnet configuration at z = 0 plane.

II.I. Magnetic Field Simulations

Magnetic field values for the selection field, $\vec{B}_s(\vec{x}) = (B_x, B_y, B_z)$, were calculated for the parameters of our in-house FFP MPI scanner shown in Fig. 1a. This scanner has two permanent disk magnets with 7-cm diameter and 2-cm thickness. The separation of the two magnets is 8 cm, with North poles facing each other (see Fig. 1b). This prototype scanner has a relatively small region where the selection field is homogeneous. Hence, it is suitable for investigating the warping effects.

For the simulation of ideal selection field, Eqn. 1 was used:

$$\vec{B}_s(\vec{x}) = \mathbf{G}\vec{x} \tag{1}$$

Here, $\vec{x}$ is position in space and $\mathbf{G}$ is the gradient matrix. For the ideal case, $\mathbf{G}$ is diagonal with trace($\mathbf{G}$) = 0. Taking the values at the iso-center of our FFP MPI scanner as reference, $(G_{xx}, G_{yy}, G_{zz}) = (2.4, 2.4, -4.8)$ T/m was used. For the non-ideal case, the selection field of our FFP scanner was numerically calculated in an 8×8×8 cm^3 region-of-interest (ROI) using COMSOL 5.1. Accordingly, the above-mentioned magnet configuration was created in COMSOL, and the fields were computed based on Amperes' Law using the AC/DC Module. The magnet grade was chosen as N38, so that the simulated fields match the measured fields of our in-house FFP MPI scanner at the iso-center [11]. The simulations used a discretization of $\Delta x = 1$ mm, $\Delta y = 1$ mm, and $\Delta z = 2$ mm along the x-, y-, and z-directions, respectively. The simulated magnetic fields and the corresponding gradients in x-, y-, and z-directions are shown in Fig. 2, together with the ideal cases, at $z = 0$ plane. The non-linearity of the selection field and degradation in gradients away from the scanner center can be clearly seen. While G_{xx} at the scanner iso-center is 2.4 T/m, it falls down to 1.4 T/m approximately 2-cm away from the center.

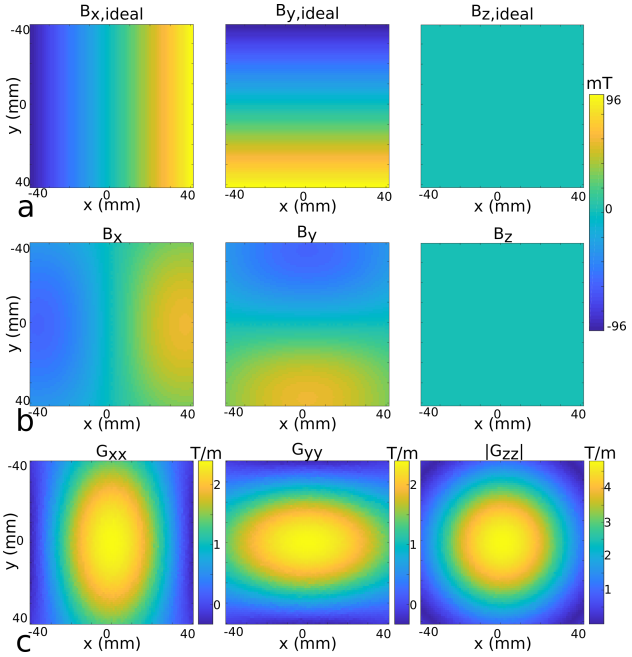

Figure 2: Selection fields in x-, y-, and z-directions at z = 0 plane, a) for the ideal case with constant G_{xx}, G_{yy}, and G_{zz}, and b) for the non-ideal case based on our FFP scanner in Fig. 1. c) The corresponding selection field gradients for the non-ideal case at z = 0 plane. The non-linearity of the selection field and the degradation in gradients are visible in regions away from the scanner iso-center.

II.II. Imaging Simulations

Imaging simulations were performed using an in-house MPI simulation toolbox in MATLAB (Mathworks, Natick, MA). The phantom consisted of point source superparamagnetic iron oxide nanoparticles (SPIOs) placed at 10 mm equidistant separations in the FOV. This phantom was then placed at the center of the permanent magnet configuration, as depicted in Fig. 1b. The following drive field parameters were utilized: 20 mT at 25 kHz along the x-direction, corresponding to a theoretical partial FOV (pFOV) size of 16.7 mm for the ideal case. Since noise effects were not investigated, a relatively small pFOV overlap percentage of 20% was utilized. A realistic nanoparticle diameter of 25 nm was assumed [15], and relaxation effects were ignored. The overall FOV was 4 × 4 cm^2 at $z = 0$ plane. The FOV was scanned in a line-by-line fash-

ion along the x-direction, with a spacing of 1 mm along the y-direction. The MPI signal, $s(t)$, was computed using the following [16]:

$$s(t) = \left(\int_{FOV} -\mu_0 \frac{\partial \vec{m}(\vec{x},t)}{\partial t} c(\vec{x}) dV \right) \cdot \vec{\rho}^{R}(\vec{x}) \quad (2)$$

In the volume integral, $c(\vec{x})$ is the nanoparticle distribution in the FOV, μ_0 is the free space magnetic permeability, and $\vec{m}(\vec{x},t)$ is the average of the magnetic moment of nanoparticles at position $\vec{x}$ at time t. Also, "$\cdot$" represents dot product operation, and $\vec{\rho}^{R}(\vec{x})$ is the sensitivity of the receiver coil taken as $(1,0,0)$ in this work (i.e., a receive coil sensitive to magnetization changes along the x-axis, with constant homogeneity).

After filtering out the fundamental harmonic of the signal, x-space images were obtained using pFOV-based x-space reconstruction with speed compensation and DC recovery [13, 14]. While the signal computation incorporated selection field non-idealities, the image reconstruction steps ignored them. Hence, an ideal selection field was assumed when computing the instantaneous position of the FFP. For the purposes of this work, the reconstruction process did not involve any image deconvolution steps.

II.III. Displacement Map Calculations

When the underlying selection-field deviates from the ideal case, geometric warping effects are expected to occur. The actual instantaneous position of the FFP can be found by computing the position $\vec{x}$ that satisfies the following equality:

$$\vec{B}_{\text{total}}(\vec{x},t) = \vec{B}_s(\vec{x}) + \vec{B}_f + \vec{B}_d(t) = 0 \quad (3)$$

Here, $\vec{B}_f$ is the focus field and $\vec{B}_d(t)$ is the drive field, both assumed to be homogeneous in space. Since we are mainly interested in the central position of the pFOV, we can use $B_d(t) = 0$. For the case of ideal selection field in Eqn. 1, to shift the pFOV center to a desired location $\vec{x}_d$, the following focus field must be applied:

$$\vec{B}_f = -\mathbf{G}\vec{x}_d \quad (4)$$

If the same focus field is applied in the case of non-ideal selection field, however, the FFP cannot be shifted by the desired amount. Considering an adjustment to the focus field, the difference between the actual FFP location and the desired FFP location can be found as follows:

$$\vec{B}_s(\vec{x}_d) - \mathbf{G}(\vec{x}_d + \vec{\Delta}) = 0 \quad (5)$$

$$\vec{\Delta} = \mathbf{G}^{-1}\vec{B}_s(\vec{x}_d) - \vec{x}_d \quad (6)$$

Here, $\vec{B}_s(\vec{x}_d)$ is the non-ideal selection field at $\vec{x}_d$, and $\mathbf{G}$ is the ideal gradient matrix with $\text{diag}(\mathbf{G}) = (2.4, 2.4, -4.8)$ T/m in this work. Finally, $\vec{\Delta} = (\Delta x, \Delta y, \Delta z)$ is the amount of the undesired displacement in x-, y-, and z-directions.

To validate the accuracy of this expression, we computed the displacement map by simulating the effect of warping as outlined in Fig. 3. First, a small ROI of size 1.2×1.2 cm^2 was selected within the FOV, with a point source SPIO placed at the center of the ROI, as shown in Fig. 3a. This ROI was then scanned line-by-line, with imaging parameters kept the same as when scanning the entire FOV. To obtain an image on a finer grid and facilitate FWHM measurements, 2D spline interpolation was applied. An example ideal image for an ROI and the reconstructed image for the non-ideal selection field case are given in Fig. 3b-c. Then, the distance between image peak intensity locations were quantified by comparing the resulting patch images, as marked in Fig. 3c. This procedure gives the displacements in both x- and y-directions due to the non-ideal field. Next, these steps were repeated by moving the point source SPIO to another grid point, with the ROI positioned around that point. The quiver plot for the resulting displacement map is shown in Fig. 3d.

II.IV. Unwarping via Displacement Map

The warping caused by selection field non-ideality can be corrected using unwarping algorithms. In a real-life implementation, one can either theoretically compute or experimentally measure the displacement map needed for this correction (e.g., by moving a point source sample through the FOV). According to Eqn. 6, the undesired displacement solely depends on the selection field and is independent of the nanoparticle type, trajectory, or other imaging parameters. Hence, measuring the displacement map only once on a relatively sparse grid would suffice. In either case, the displacement map is bound to be a coarse map, due to either discretization of the simulation grid or scan time limitations. We have observed that a 3rd degree polynomial suffices to accurately characterize the displacement in both directions. After polynomial fitting, a much finer displacement map can be used for unwarping the reconstructed image. Here, a geometric transformation was implemented by using MATLAB's built-in *imwarp* function, which takes the reconstructed image and pixel-wise displacement map as the inputs, and outputs the corrected image. This unwarping algorithm finds the corrected intensity at a given pixel through inverse mapping, i.e., by mapping the given pixel location to the corresponding location in the reconstructed image, and computing the pixel intensity via interpolation. This procedure ensures that there will be no gaps or overlaps in the corrected image.

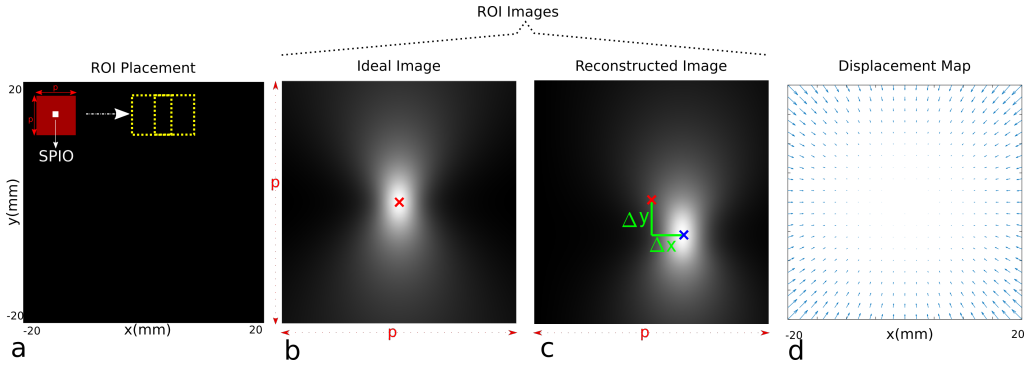

Figure 3: a) The FOV is partitioned into ROIs with size $p \times p$ mm^2, which are used one at a time. A point source SPIO is placed in the center of the selected ROI. b) Image from the red patch (selected ROI) for the case of ideal selection field. The red cross indicates the peak intensity position. c) Reconstructed image of the same patch for the case of non-ideal selection field. Here, the blue cross indicates the peak intensity position, while the red cross marks the same position as in (b). Δx and Δy are the distances between these two crosses in x- and y-directions, respectively. d) The quiver plot of the displacement map across the entire 4×4 cm^2 FOV (shown here for a low-resolution 2×2 mm^2 grid for display purposes).

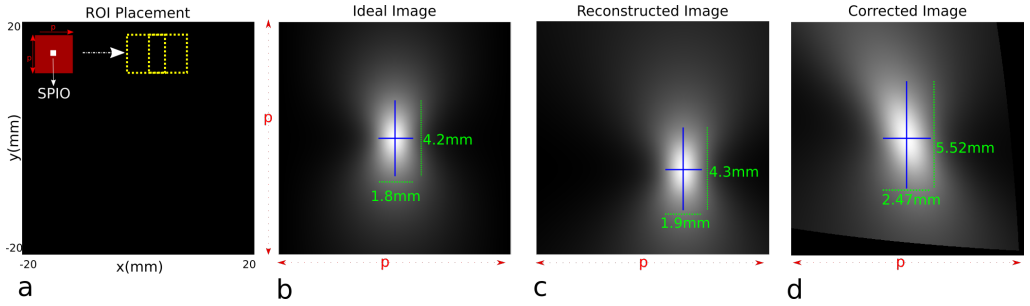

Figure 4: a) The FOV is partitioned into ROIs, with a point source SPIO placed at the center of the selected ROI. b) Image from the red patch for the case of ideal selection field. The blue lines indicate the FWHM measurements, with the corresponding values provided in green. c) The reconstructed image in the case of non-ideal selection field. The FWHM measurements yield similar values as in the ideal case. d) The corrected image after unwarping displays a loss in resolution in both directions.

II.V. Resolution Loss Calculations

The resolution in x-space MPI changes linearly with the term G^{-1} and is anisotropic [2, 3]. It was shown that the resolution in the tangential direction (i.e., the direction in which the drive field is applied) is better than the resolution in the normal direction (i.e., the direction orthogonal to the drive field). In this work, the tangential and normal directions correspond to x- and y-directions, respectively. Accordingly, the FWHM resolutions for these two directions can be approximated as [3]:

$$\text{FWHM}_x \approx \frac{25 k_B T}{\pi M_{\text{sat}}} G_{xx}^{-1} d^{-3} \tag{7}$$

$$\text{FWHM}_y \approx \frac{57 k_B T}{\pi M_{\text{sat}}} G_{yy}^{-1} d^{-3} \tag{8}$$

Here, k_B is Boltzmann's constant, T is absolute temperature, d is the nanoparticle diameter, and M_{sat} is the saturation magnetization of the nanoparticle. For the ideal selection field case, the gradient values of $G_{xx} = 2.4$ T/m and $G_{yy} = 2.4$ T/m correspond to theoretical resolutions of $\text{FWHM}_x = 1.8$ mm and $\text{FWHM}_y = 4.2$ mm, respectively. In the non-ideal case, however, both gradient values change with position, yielding a position-dependent resolution inside the FOV. More specifically, the resolution worsens in both directions in regions away from the scanner iso-center due to the degradation in selection field gradients (see Fig. 2c). Still, the resolution at a given position can be computed via Eqns. 7 and 8 using the actual gradient values at that position. These gradients can be computed from a measured or simulated selection field map via partial derivatives, i.e., $G_{ii} = \partial B_{s,i} / \partial i$, where i is x or y.

To validate the expressions in Eqns. 7 and 8, the resolution maps of ideal, reconstructed, and corrected images were computed using the approach outlined in Fig. 4. Following a similar approach as in the displacement map computation, a point source SPIO was placed

at a predetermined grid location. In the same fashion as before, the ideal image and reconstructed image were obtained. This time, the reconstructed image was also corrected using the displacement map. Then FWHM values in both x- and y-directions were measured as shown in Fig. 4b-d. This procedure was repeated at all grid locations to obtain position-dependent resolution maps. Interestingly, the reconstructed image displays a point source with almost identical FWHM value as in the ideal case. The resolution loss is only visible in the corrected image after unwarping.

II.VI. Comparison to Direct Reconstruction

The above-mentioned x-space reconstruction first ignored selection field non-ideality, then corrected its effects via unwarping the reconstructed image. For comparison purposes, we have also performed a direct x-space reconstruction by computing the actual FFP position at all time points, i.e., by numerically computing $\vec{x}$ that satisfies $\vec{B}_{\text{total}}(\vec{x},t)=0$. To obviate the need for DC recovery, the fundamental harmonic was not filtered out in these simulations. Next, the speed-compensated MPI signal was assigned to actual FFP positions, followed by scattered interpolation to obtain a 2D image on a Cartesian grid.

III. Results

III.I. Warping Artifact

The x-space MPI images of a 2D phantom shown in Fig. 5a are obtained under ideal and non-ideal selection fields. The resulting images are given in Fig. 5b and Fig. 5c, respectively. In the “reconstructed image", i.e., the image due to non-ideal selection field, the point sources are misregistered, resulting in an apparent warping. This effect manifests itself more dramatically when the samples are further away from the center of the scanner. The point sources lying at the edges of the FOV are pushed towards the center, as indicated by the red arrows. Hence, if there were SPIOs outside but close to the edge of the FOV, they would have been mapped to positions inside the FOV due to this warping.

III.II. Displacement Map Results

The result of the displacement map calculations are given in Fig. 6 for both the theoretical displacements computed using Eqn. 6 and for simulated displacements calculated as outlined in Fig. 3. The first thing to note is that there is negligible displacement at central locations. The displacement increases away from the center of the scanner, as the field deviates from the ideal case. At the corner

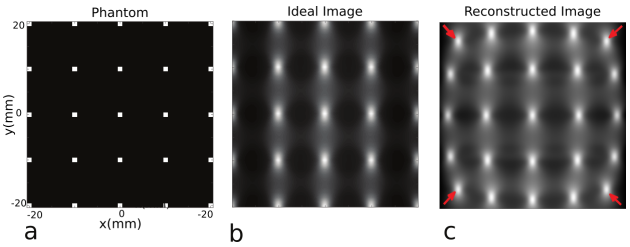

Figure 5: a) Phantom with point source SPIOs placed at 10 mm separations. b) Image for the ideal selection field, and c) x-space reconstructed MPI image for the case of non-ideal selection field.

of the 4×4 cm^2 FOV, the displacement is around 4 mm in both x- and y- directions, corresponding to approximately 5.7 mm displacement along the diagonal direction. Importantly, the displacements are such that the points are always pushed towards the center of the scanner. In other words, a non-ideal selection field causes us to actually scan a wider FOV than intended, which implies that a corrected image of the targeted FOV can be achieved after unwarping.

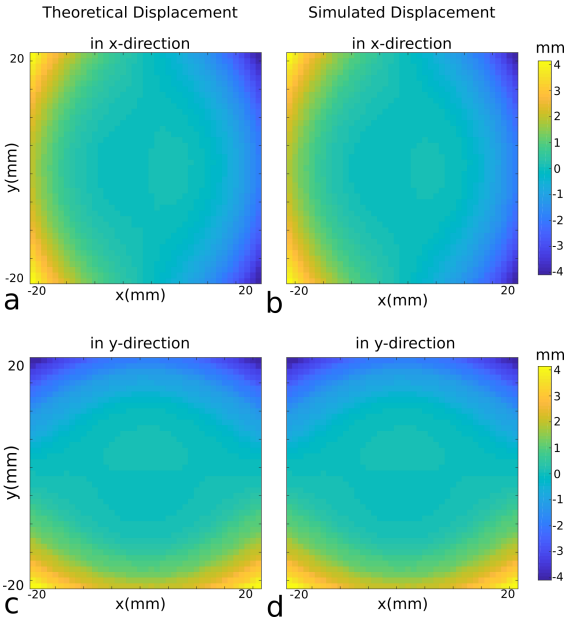

Figure 6: a) Theoretical and b) simulated displacement maps in x-direction, and c) theoretical and d) simulated displacement maps in y-direction. Here, the theoretical values were computed via Eqn.6, and simulated values were computed as described in Fig.3.

Another important result of Fig. 6 is that the theoretical and simulated displacements agree excellently, aside from negligible errors stemming from discretization. The normalized root-mean-square errors (NRMSE) between the theoretical and simulated cases are 2.7%

and 5.2% for displacements in x- and y-directions, respectively (calculated across the displayed maps in Fig. 6). Hence, in a real-life scenario, if one knows the magnetic field map for the selection field, there would not be a need to perform a calibration measurement to determine the displacement map. The selection field map could be computed using simulation tools such as COMSOL (as done in this work) or using analytical expressions that exploit the symmetry of the magnet configuration [17]. Alternatively, as is standard practice in MPI, one can directly measure the selection field map (e.g., using Hall effect probes) [11, 18].

III.III. Resolution Loss Results

Fig. 7 gives the results of the resolution map for both the theoretical case computed using Eqns. 7 and 8, and for the simulated case explained in Fig. 4. Here, the values for the simulated case correspond to the FWHM resolutions measured after unwarping. The theoretical and simulated cases agree quite well, except for ringing-like features seen in the simulated resolution maps, which potentially stem from FWHM measurements in a discretized setting. The NRMSEs between the theoretical and simulated cases are 2.3% and 4.3% for resolutions in x- and y-directions, respectively (calculated across the displayed maps in Fig. 7).

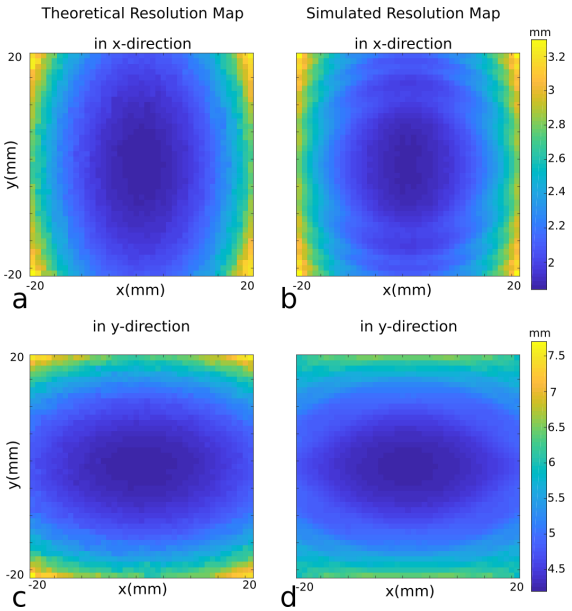

Figure 7: a) Theoretical and b) simulated resolution maps in x-direction, and c) theoretical and d) simulated maps in y-direction. The theoretical maps were computed using Eqns. 7 and 8, and the simulated maps were computed as described in Fig. 4.

As expected, the resolutions at the center of the scanner are 1.8 mm and 4.2 mm along the x- and y-directions, respectively. The resolution worsens away from the center of the scanner. At the corner of the 4×4 cm^2 FOV, the simulated resolutions are 3.3 mm and 6 mm in x- and y-directions, respectively.

III.IV. Unwarping Results

The 3rd degree polynomial fitting to the individual displacement maps are shown in Fig. 8a and b. The black marks indicate the measured results at the grid locations. Since magnetic fields do not change abruptly, the displacements are also smooth and slowly changing functions.The NRMSEs between the fitted and measured displacements are 2.4% and 5.1% in x- and y-directions, respectively, verifying that a 3rd degree polynomial with 9 coefficients suffices to describe these smooth functions. With the finer displacement map obtained after polynomial fitting, a corrected image of the 2D phantom is obtained, as shown in Fig. 8c. In the corrected image, the point sources positioned at the edges of the FOV are all mapped back to their original positions. As expected, there is a loss of resolution towards the edges of the FOV. Note that this resolution loss is not induced by the unwarping algorithm, but is caused by the non-ideality in selection field gradients, as discussed in Section II.V and in Section III.III.

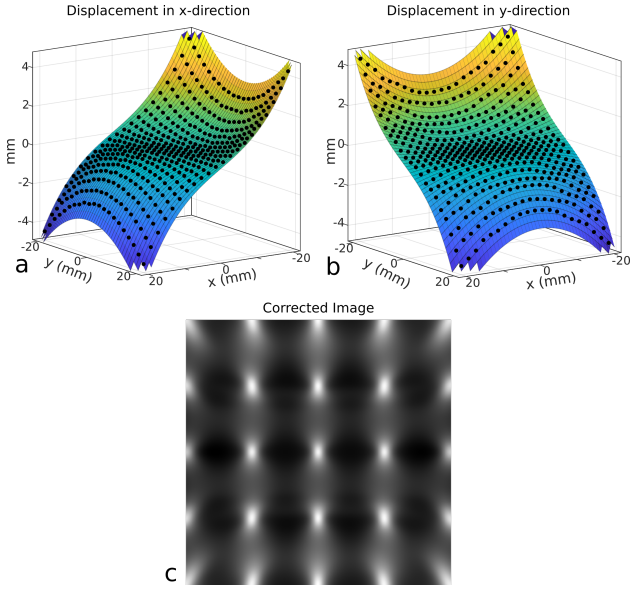

Figure 8: Results of 3^{rd} degree polynomial fitting for the displacement maps in a) x-direction and b) y-direction. The black marks indicate the measured results at the simulated grid locations. c) The corrected version of the image in Fig. 5c, after unwarping using the fitted displacement maps.

III.V. Direct Reconstruction Results

To validate that the resolution loss in Fig. 8c is not caused by the unwarping algorithm, we have next performed a direct x-space reconstruction by computing the actual FFP position at all time points. First, Fig. 9a-b shows how the line-by-line scanning trajectory is warped in the non-ideal selection field case, extending beyond the targeted FOV. Figure 9c displays the direct x-space reconstructed image, in the region corresponding to the intended FOV. This image closely matches the corrected image in Fig 8c, verifying that it is the non-ideality of the selection field that causes the loss of resolution towards the edges of the FOV.

In the ideal trajectory, the drive and receive directions are collinear (i.e., both are along the x-axis), and hence the MPI signal is governed by the collinear point spread function (PSF) only [3]. On the other hand, the warped trajectory causes the receive coil along the x-axis to pick up an MPI signal that has contributions from both the collinear and the transverse PSFs, where the latter is known to induce blurring along the diagonal directions [3, 19]. Note that the contribution of the transverse PSF increases as the trajectory curves further away from the x-axis, leading to a noticeable diagonal blurring towards the corners of the FOV.

III.VI. Demonstration on a Vasculature Phantom

To demonstrate both the manifestation of the non-ideal selection field induced artifacts and the effectiveness of the unwarping algorithm on a more complex case, imaging simulations were performed using the vasculature phantom shown in Fig. 10a. Here, the phantom was designed such that it extends beyond the targeted 4×4 cm^2 FOV. All simulation parameters were kept the same as before (see Section II.II). The images under ideal and non-ideal selection fields are displayed in Fig. 10b-c, respectively. In the reconstructed image, some of the branches of the vasculature phantom that are outside the targeted FOV are pushed into the image due to warping (see the red arrows in Fig. 10c). Next, the reconstructed image was unwarped using the displacement maps in Fig. 8a-b. As shown in the corrected image in Fig. 10d, the branches near the edges/corners of the FOV are successfully mapped back to their correct positions. For this more complex case, the resolution loss towards the edges of the FOV is not as noticeable as that in Fig. 8c.

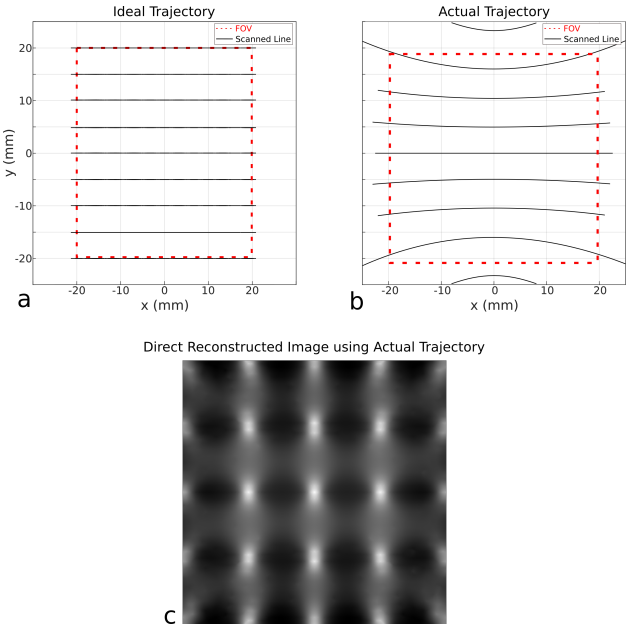

Figure 9: The line-by-line scan trajectory for the case of a) ideal selection field and b) non-ideal selection field, showing every fifth line. The targeted FOV was 4×4 cm^2 (marked with the dashed red square). In the non-ideal case, the trajectory warps in regions away from the scanner isocenter, extending outside the intended FOV. c) The direct x-space reconstructed image using the actual FFP trajectory closely matches the corrected image in Fig. 8c.

IV. Discussion

The results in this work show that a geometric warping artifact occurs in x-space reconstructed images, if the targeted FOV extends beyond the linear region of the selection field. These artifact occur due to a combination of two factors: selection field non-linearity, combined with a focus field and drive field that ignores this non-ideality. Hence, instead of the unwarping method presented in this work, one can also adjust the focus field and drive field amplitudes to counteract the effects of the selection-field non-ideality. Note that while this would alleviate the warping problem, the resolution loss away from the center of the scanner would still be observed.

Alternatively, instead of using a focus field, one may move the phantom/subject along the bore of the scanner (i.e., in a sliding-table fashion) to remain in the linear region of the selection field. Such an approach was previously proposed for the purposes of enlarging the FOV, as an alternative to the focus field [20]. Accordingly, this solution would also alleviate the resolution loss issue. In a realistic setting, however, this technique can only fix the warping along the scanner bore direction.

In Fig. 4, the reconstructed image before unwarping displayed almost identical FWHM value as in the ideal case. The reason for this phenomenon is the fact that we used FWHM to quantify the resolution. In addition to a resolution loss, the image is also experiencing warping, and these two effects counteract each other to yield almost identical PSF shape in the warped coordinate

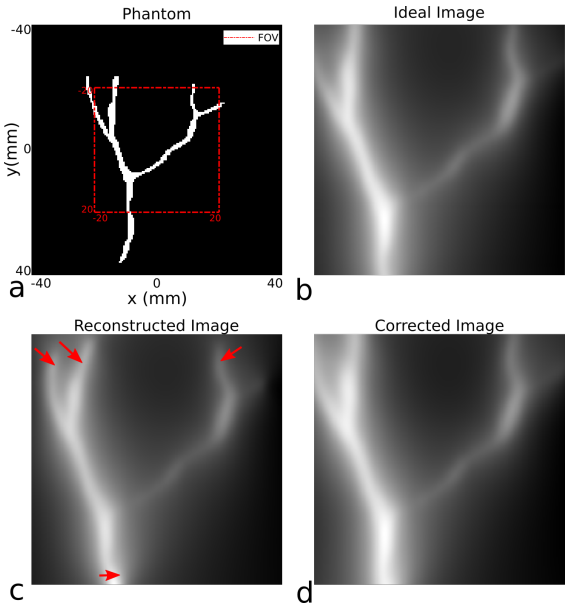

Figure 10: a) A vasculature phantom extending beyond the targeted 4×4 cm^2 FOV (dashed red box). b) Image for the ideal selection field, c) x-space reconstructed image for the non-ideal selection field, and d) corrected image after unwarping.

frame. If we instead use separability of two point sources as the resolution metric, the loss in resolution would be clear even in the warped image. While each point source would have the same FWHM in the warped image, they would be brought closer because of warping, making it harder and harder to separate them at positions away from the center of the scanner. In theory, using the separability metric for the quantification of resolution should yield identical results as the FWHM measured *after* unwarping.

If the selection field is known, one can compute the actual FFP trajectory and perform a direct x-space reconstruction, as shown in Fig. 9c. It should be mentioned that this approach is not practical, since the actual FFP trajectory would need to be recomputed every time a drive field parameter (i.e., frequency, amplitude, and/or trajectory type) is changed. Furthermore, because pFOVs lie on warped lines as shown in Fig. 9b, a pFOV-overlap-based DC recovery algorithm can become computationally more challenging. In contrast, the displacement map is independent of the trajectory, and the DC recovery algorithm is straightforward if we assume a straight line. Hence, it is considerably more practical to perform x-space reconstruction by ignoring selection field non-ideality, and then correcting its effects via unwarping, as done in Fig. 8c.

A previous work proposed a hybrid solution where a system function approach was adapted to x-space images to counteract the warping effects [21]. Accordingly, the PSF (or its Fourier transform) measured at each pixel position was inserted into an image-based system matrix, which was then used during the image reconstruction step. Note that the system matrix in that case depends on not just the scanner setup, but also the nanoparticle characteristics. In contrast, the unwarping approach presented in this work solely depends on the selection field and is independent of the nanoparticle type.

We expect the unwarping approach to work successfully as long as the FOV does not extend too far outside the linear region and into the near-constant selection field region. If the selection field gradient falls down to zero, signals from different positions would be mapped to the same location in the reconstructed image. In such a case, an unwarping algorithm (or direct reconstruction) would fail to separate those signals. Hence, one needs to remain in a region where the selection field maintains a non-zero gradient. As seen in Fig. 8, the unwarped image reflects the positions of the point sources accurately, albeit with a resolution loss near the edges of the FOV. Hence, while warping effects can be corrected, resolution loss is inherent to how it scales with the gradient. Therefore, the size of the FOV may need to be chosen to maintain a target resolution.

This work incorporated the effects of selection-field-induced artifacts only. Previous works considered the effects of transmit/receive coil non-idealities [10, 22]. It remains an important future work to investigate the effects of those additional non-idealities on x-space reconstruction, and to find the trade-off between hardware fidelity and image quality.

V. Conclusions

In this study, non-ideal selection-field-induced artifacts in x-space MPI are demonstrated via both theoretical derivations and imaging simulations. The image warping can take place when the FOV is enlarged, such that the gradient of the selection field is no longer constant. This situation arises if the system is not specifically designed for high fidelity linearity in a large volume. The resulting distortion, however, is relatively benign and a corrected image can be obtained using image unwarping algorithms. The resolution loss, on the other hand, remains in the unwarped image and may be the determining factor for the size of the FOV.

Acknowledgments

This work was supported by the Scientific and Technological Research Council of Turkey (TUBITAK 217S069).

References

[1] B. Gleich and J. Weizenecker. Tomographic imaging using the nonlinear response of magnetic particles. *Nature*, 435(7046):1214–1217, 2005. doi: 10.1038/nature03808.

[2] P. W. Goodwill and S. M. Conolly. The X-Space Formulation of the Magnetic Particle Imaging Process: 1-D Signal, Resolution, Bandwidth, SNR, SAR, and Magnetostimulation. *IEEE Transactions on Medical Imaging*, 29(11):1851–1859, 2010. doi: 10.1109/tmi.2010.2052284.

[3] P. W. Goodwill and S. M. Conolly. Multidimensional x-space magnetic particle imaging. *IEEE Transactions on Medical Imaging*, 30(9):1581–1590, 2011. doi: 10.1109/TMI.2011.2125982.

[4] P. Vogel, M. A. Rückert, P. Klauer, W. H. Kullmann, P. M. Jakob, and V. C. Behr. Traveling wave magnetic particle imaging. *IEEE Transactions on Medical Imaging*, 33(2):400–407, 2014. doi: 10.1109/TMI.2013.2285472.

[5] J. Rahmer, J. Weizenecker, B. Gleich, and J. Borgert. Signal encoding in magnetic particle imaging: properties of the system function. *BMC Medical Imaging*, 9(4):485–491, 2009. doi: 10.1186/1471-2342-9-4.

[6] F. Roméo and D. I. Hoult. Magnet field profiling: Analysis and correcting coil design. *Magnetic Resonance in Medicine*, 1(1):44–65, 1984. doi: 10.1002/mrm.1910010107.

[7] A. Weber, F. Werner, J. Weizenecker, T. Buzug, and T. Knopp. Artifact free reconstruction with the system matrix approach by overscanning the field-free-point trajectory in magnetic particle imaging. *Physics in Medicine and Biology*, 61(2):475–487, 2015. doi: 10.1088/0031-9155/61/2/475.

[8] J. Kybic, P. Thevenaz, A. Nirkko, and M. Unser. Unwarping of unidirectionally distorted EPI images. *IEEE Transactions on Medical Imaging*, 19(2):80–93, 2000. doi: 10.1109/42.836368.

[9] S. J. Doran, L. Charles-Edwards, S. A. Reinsberg, and M. O. Leach. A complete distortion correction for MR images: I. Gradient warp correction. *Physics in Medicine and Biology*, 50(7):1343–1361, 2005. doi: 10.1088/0031-9155/50/7/001.

[10] H. Medimagh, P. Weissert, G. Bringout, K. Bente, M. Weber, K. Grafe, A. Cordes, and T. M. Buzug. Artifacts in field free line magnetic particle imaging in the presence of inhomogeneous and nonlinear magnetic fields. *Current Directions in Biomedical Engineering*, 1(1):245–248, 2015. doi: 10.1515/CDBME-2015-0061.

[11] M. Utkur, Y. Muslu, and E. U. Saritas. A 4.8 T/m Magnetic Particle Imaging Scanner Design and Construction. 2017. doi: 10.1109/BIYOMUT.2017.8479214.

[12] Y. Muslu, M. Utkur, O. B. Demirel, and E. U. Saritas. Calibration-free relaxation-based multi-color magnetic particle imaging. *IEEE Transactions on Medical Imaging*, 37(8):1920–1931, 2018. doi: 10.1109/TMI.2018.2818261.

[13] K. Lu, P. W. Goodwill, E. U. Saritas, B. Zheng, and S. M. Conolly. Linearity and shift invariance for quantitative magnetic particle imaging. *IEEE Transactions on Medical Imaging*, 32(9):1565–1575, 2013. doi: 10.1109/tmi.2013.2257177.

[14] E. Bozkurt and E. U. Saritas. Signal-to-noise ratio optimized image reconstruction technique for magnetic particle imaging. *Journal of the Faculty of Engineering and Architecture of Gazi University*, 32(3):999–1013, 2017. doi: 10.17341/gazimmfd.337864.

[15] R. M. Ferguson, A. P. Khandhar, S. J. Kemp, H. Arami, E. U. Saritas, L. R. Croft, J. Konkle, P. W. Goodwill, A. Halkola, J. Rahmer, J. Borgert, S. M. Conolly, and K. M. Krishnan. Magnetic particle imaging with tailored iron oxide nanoparticle tracers. *IEEE Transactions on Medical Imaging*, 34(5):1077–1084, 2015. doi: 10.1109/TMI.2014.2375065.

[16] T. Knopp and T. M. Buzug. *Magnetic Particle Imaging: An Introduction to Imaging Principles and Scanner Instrumentation*. Springer, Berlin/Heidelberg, 2012.

[17] S. I. Babic and C. Akyel. Improvement in the analytical calculation of the magnetic field produced by permanent magnet rings. *Progress In Electromagnetics Research C*, 5:71–82, 2008.

[18] P. W. Goodwill, J. J. Konkle, B. Zheng, E. U. Saritas, and S. M. Conolly. Projection x-space magnetic particle imaging. *IEEE Transactions on Medical Imaging*, 31(5):1076–1085, 2012. doi: 10.1109/TMI.2012.2185247.

[19] A. A. Ozaslan, A. Alacaoglu, O. B. Demirel, T. Çukur, and E. U. Saritas. Fully automated gridding reconstruction for non-Cartesian x-space magnetic particle imaging. *Physics in Medicine & Biology*, 64(16):165018, 2019. doi: 10.1088/1361-6560/ab3525.

[20] P. Szwargulski, N. Gdaniec, M. Graeser, M. Möddel, F. Griese, K. M. Krishnan, T. M. Buzug, and T. Knopp. Moving table magnetic particle imaging: A stepwise approach preserving high spatio-temporal resolution. *Journal of Medical Imaging*, 5(4):1, 2018. doi: 10.1117/1.JMI.5.4.046002.

[21] P. Vogel, T. Kampf, M. A. Ruckert, and V. C. Behr. Flexible and dynamic patch reconstruction for traveling wave magnetic particle imaging. *International Journal on Magnetic Particle Imaging*, 2(2), 2016. doi: 10.18416/ijmpi.2016.1611001.

[22] K. Murase, N. Banura, A. Mimura, and K. Nishimoto. Simple and practical method for correcting the inhomogeneous sensitivity of a receiving coil in magnetic particle imaging. *Japanese Journal of Applied Physics*, 54(3):038001, 2015. doi: 10.7567/jjap.54.038001.